Supplemental Material:

Vibronic response of a spin-1/2 state from a carbon impurity in two-dimensional WS_2

Katherine A. Cochrane,[1,*] Jun-Ho Lee*,[1,2] Christoph Kastl,[3] Jonah Haber,[1,2] Tianyi Zhang,[4,5] Azimkhan Kozhakhmetov,[4] Joshua A. Robinson,[4,5] Mauricio Terrones,[4,5,6] Jascha Repp,[7] Jeffrey B. Neaton,[1,2,8,†] Alexander Weber-Bargioni,[1,‡] and Bruno Schuler[1,9,§]

[1] *Molecular Foundry, Lawrence Berkeley National Laboratory, California 94720, USA*

[2] *Department of Physics, University of California at Berkeley, Berkeley, CA 94720, USA*

[3] *Walter-Schottky-Institut and Physik-Department,*
Technical University of Munich, Garching 85748, Germany

[4] *Department of Materials Science and Engineering,*
The Pennsylvania State University, University Park, PA 16082

[5] *Center for Two-Dimensional and Layered Materials,*
The Pennsylvania State University, University Park, PA, 16802

[6] *Department of Physics and Department of Chemistry,*
The Pennsylvania State University, University Park, PA, 16802

[7] *Institute of Experimental and Applied Physics,*
University of Regensburg, Regensburg, Germany

[8] *Kavli Energy Nanosciences Institute at Berkeley, Berkeley, CA 94720, USA*

[9] *nanotech@surfaces Laboratory, Empa – Swiss Federal Laboratories*
for Materials Science and Technology, Dübendorf, Switzerland

(Dated: October 7, 2020)

CONTENTS

SUPPLEMENTARY EXPERIMENTS

Comparison of monolayer vs bilayer WS_2

In this study, we examined carbon substituting chalcogen (C_X) defects in several transition metal dichalcogenides (TMDs), including monolayer (1ML) and bilayer (2ML) tungsten disulfide (WS_2). The majority of the sample coverage of the chemical vapor deposition (CVD) grown WS_2 was 1 or 2 monolayers, but small, multilayer terraces sometimes grew in the center of the ~ 20 micron TMD islands. An edge of such a multilayer area is observed in Fig. S1a. In this image, the lowest terrace is 1ML WS_2 and each step is an increase in 1ML up to 6ML. A step profile is shown in Fig. S1b.

When WS_2 is reduced to 1ML the previously indirect band gap becomes direct with band extrema at different points of the Brillouine zone. This leads to different features in scanning tunneling spectroscopy (STS) measurements, particularly the onset of the conduction and valence bands. It should be noted that the onset of the valence band of 1ML WS_2 can only be observed from close distances as the K states have a reduced tunnelling matrix and the spectrum is therefore dominated by the Γ states[1]. As is seen with WS_2,[1] a narrowing of the band gap is observed with increasing film thickness, Fig. S1c.

Scanning tunneling spectra along a line of C_S in 1ML and 2ML WS_2 are shown in Fig. S2a and b respectively. Besides the change in the electron-phonon coupling strength discussed in the main text, additional resonances are observed above the valence band edge that can be attributed to resonant and bound states of the Coulomb impurity[2] .Because the screening and contributions from the local band extrema are different, the binding energy and the character of these states vary between 1ML and 2ML as expected.

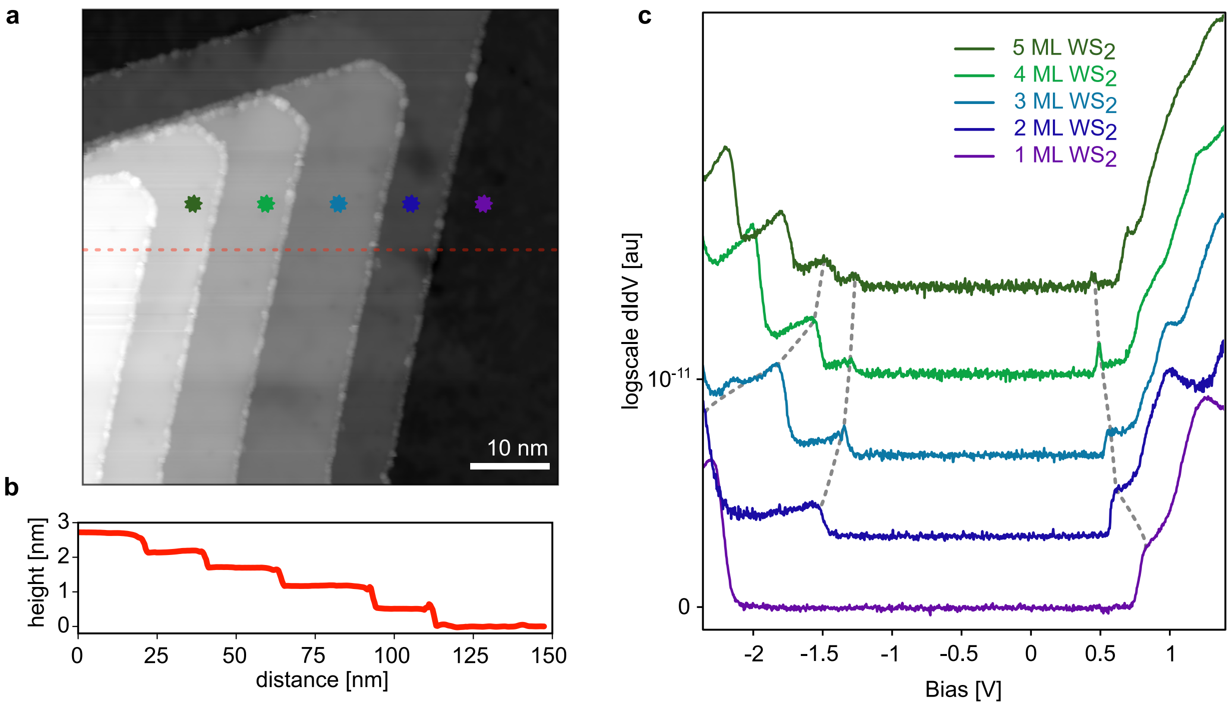

Figure S1. **a**, STM of a WS_2 island showing terraces of 1 to 6 ML, $V_B = 1.5$ V, $I_t = 1$ nA, 150 x 150 nm. **b**, Height profile along the dashed red line indicated in (**a**). Average step height between terraces is approximately 0.5 nm. **c**, STS of 1 - 5 ML WS_2, setpoint V_B = 1.5 V, I_t = 1 nA, and V_{mod} = 10 mV.

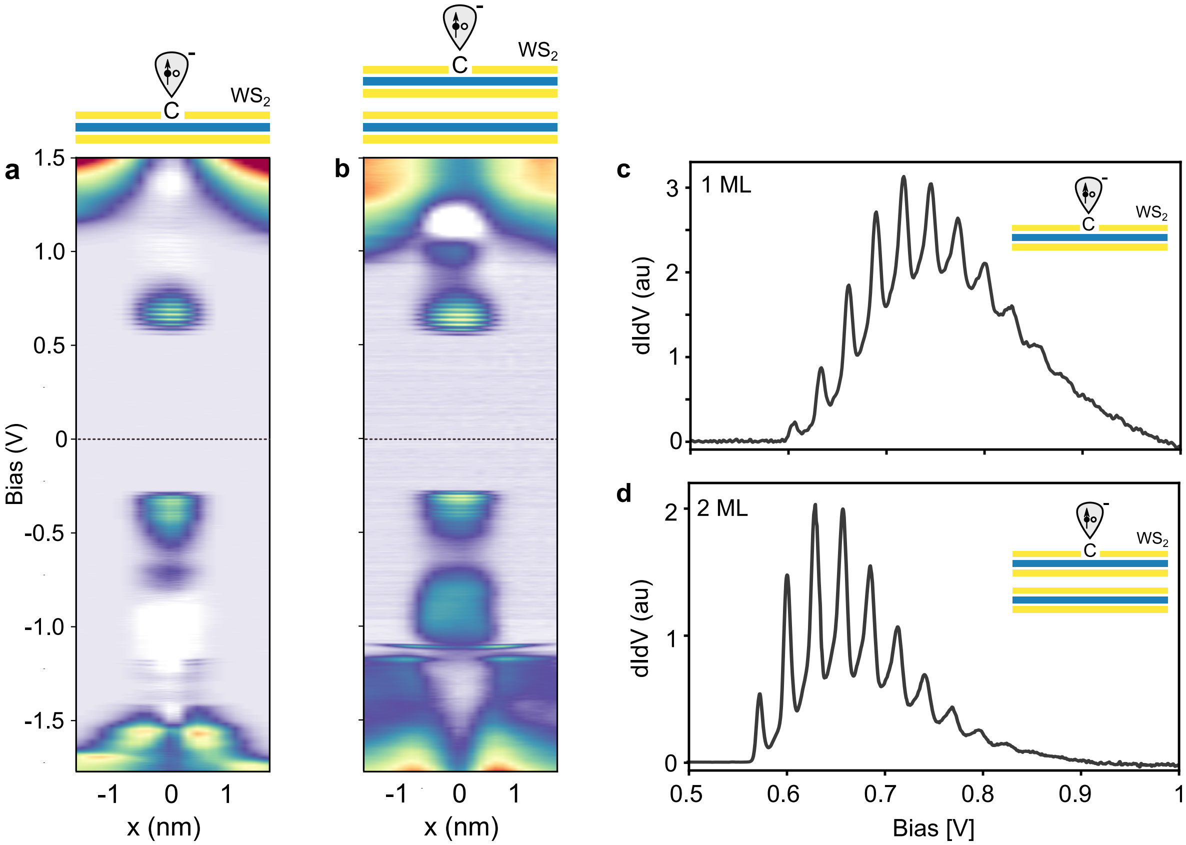

Figure S2. **Comparison of tunneling spectra of a C_S defect on monolayer and bilayer WS_2. a,b**, Constant height point by point tunneling spectra acquired across the defect on monolayer (**a**) and bilayer (**b**) WS_2. Dotted black line indicates the Fermi energy. **c,d**, Point spectra of the converted defect on monolayer (**c**) and bilayer (**d**) WS_2.

Majority and minority conversion events

The dehydrogenation of CH_X reproducibly occurs at applied sample biases and tunneling currents above 2.5 V and 15 nA respectively. Fig. S3a shows a $20\times20\ \mathrm{nm}^2$ area of methane plasma treated, CVD grown WS_2 before any high currents or biases were applied; only CH_S and top and bottom O_S defects are observed. After a scan with dehydrogenation parameters, the majority of the time the hydrogen was removed from the carbon (Fig. S3b). However, occasionally the entire CH complex was removed and a sulfur vacancy was created, as indicated by the red circle in Fig. S3c. This creation of a sulfur vacancy was found to be an irreversible process. In addition, when passing over previously created C_S defects, occasionally reattachment of the hydrogen was seen as indicated by the yellow circle in Fig. S3d.

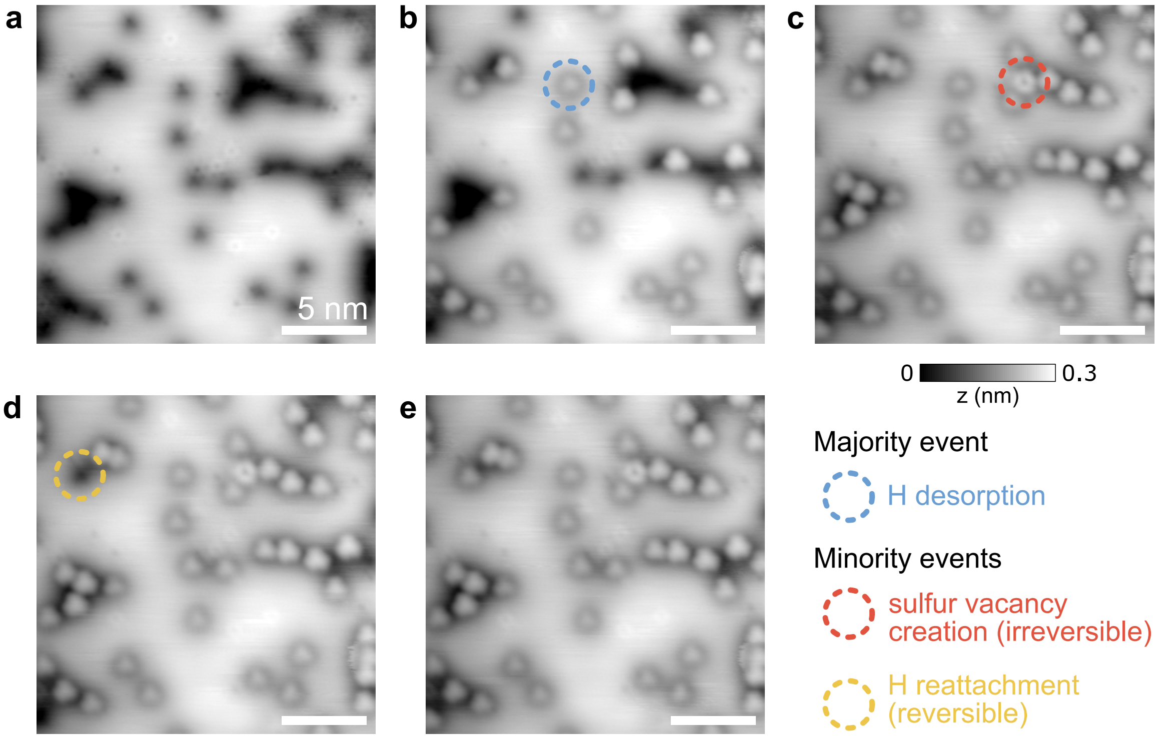

Figure S3. **a-e**, Sequential STM images taken after rastering the tip over CH_S defects while at dehydrogenation conditions of I_t =20 nA and V_B = 2.5 V. Scanning parameters: V_B = 1.2 V, I_t = 100 pA, $20\times20\ \mathrm{nm}^2$, sample was CVD grown and methane plasma doped WS_2.

High resolution imaging of $\mathrm{CH_S}$ and $\mathrm{C_S}$

Figure S4 shows a scanning tunneling microscopy overview image before and after the hydrogen removal process. After one pass with dehydrogenation parameters (biases and tunneling currents above 2.5 V and 15 nA respectively), a majority of the $\mathrm{CH_S}$ defects have been converted into $\mathrm{C_S}$ defects. Top and bottom oxygen at sulfur substitutions are also observed and remain unchanged, indicating the selectivity of the process.

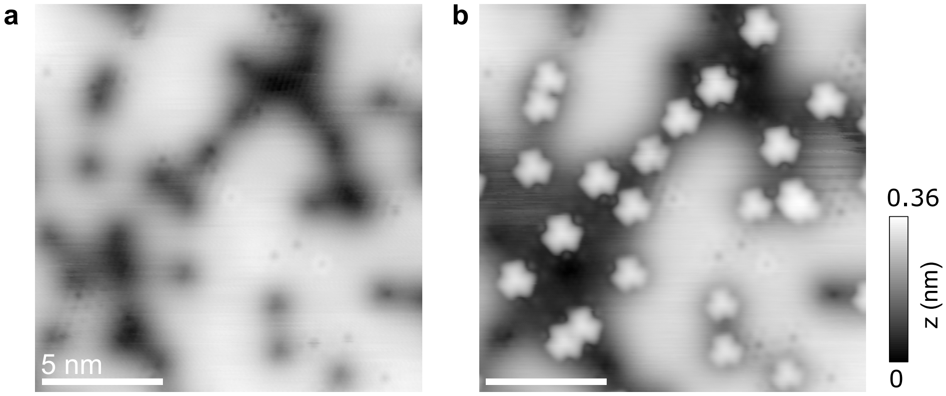

Figure S4. **a**,**b**, STM image of CH doped WS_2 before (**a**) and after (**b**) dehydrogenation by high voltage and high currents. Scanning parameters: V_B = 1.1 V, I_t = 100 pA, 20 x20 nm.

Both the $\mathrm{CH_S}$ and the $\mathrm{C_S}$ defect are negatively charged, which results in the upwards bending of the substrate conduction and valence bands. Because of this, at positive biases these defects are imaged as dark depressions (in the case of $\mathrm{CH_S}$, Fig. S5a) or with a dark depression surrounding the in-gap orbital features ($\mathrm{C_S}$, Fig. S5b). If STM topographic images of the two defects taken under identical scanning parameters are subtracted from one another, the resulting image shows only the in-gap orbital from $\mathrm{C_S}$, as seen in Fig. S5c. This indicates the degree of band banding, and therefore quantity of negative charge, is the same for both defects. The similar magnitude of band bending is also observed in the along a line tunneling spectra shown in the main paper (Fig. 3a,b).

Figure S5e shows a high resolution CO-functionalized tip AFM image of a side by side $\mathrm{CH_S}$ (left) and $\mathrm{C_S}$ (right) defect (corresponding STM of the same area is shown above in Fig. S5d). Just as in imaging of the isolated defects seen in the main text, the $\mathrm{CH_S}$ defect shows a subtle

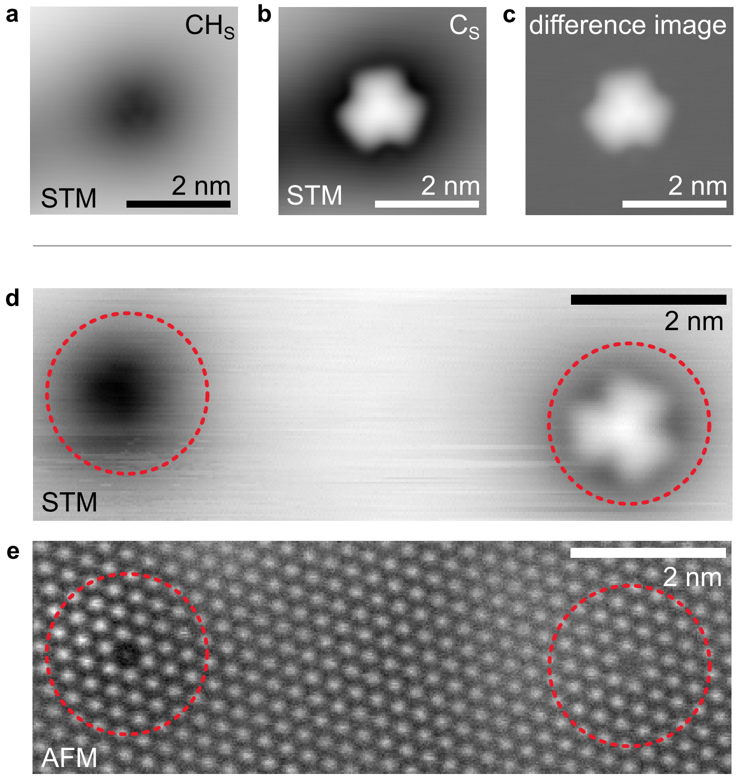

Figure S5. **a,b**, STM constant current topographic image of a CH$_S$ and a C$_S$ defect respectively, $V_B = 1.1\,\mathrm{V}$, $I_t = 100\,\mathrm{pA}$, $4\times4\,\mathrm{nm}^2$. **c**, Difference image of (**a**) and (**b**) indicating the cancellation of the dark depression around the C$_S$ defect, the component arising from the negative charge. **d**, STM and **e**, corresponding AFM images of side by side CH$_S$ and a C$_S$ defects, $9\times3\,\mathrm{nm}^2$. (STM: V_B = 0.73 V, I_t = 100 pA, AFM: V_B = 0 V).

protrusion at the chalcogen site, while the C$_S$ defect appears as a missing sulfur atom.

STS of partially occupied $C_S^{\bullet -}$ orbitals

The in gap resonances observed in the tunneling spectra of $C_S^{\bullet -}$, discussed in detail in the main text and shown again in Fig. S6a, arise from a singly occupied electronic orbital that is split into two spin-polarized states. Upon electron detachment at negative bias the defect state can be depopulated, whereas at positive bias an electron can be added to the second spin-polarized state. The measured energetic splitting between the two states result from a combination of Coulomb repulsion and spin splitting.

Spatially resolved $\mathrm{d}I/\mathrm{d}V$ maps were taken at five of the observed resonances, both above and below E_F. These maps appear spatially similar, indicating the resonances arises from the same electronic orbital.

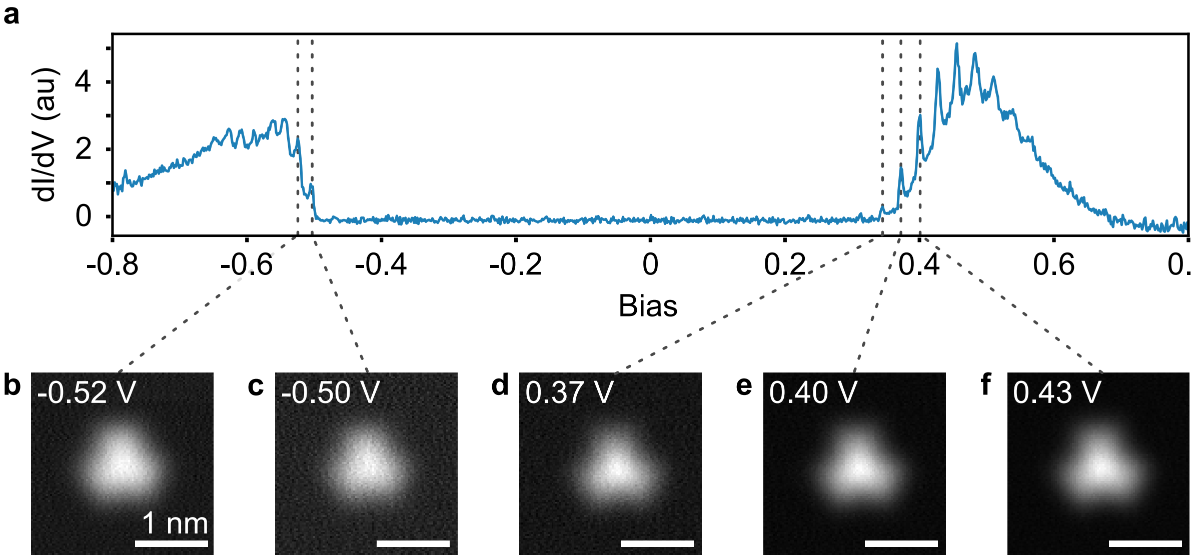

Figure S6. **a**, Scanning tunneling spectrum of a $C_S^{\bullet -}$ defect in 1ML WS_2 showing the occupied and unoccupied vibronic resonances. **b-f**, Spatially resolved STS maps of the singly occupied orbital of the C_S defect at negative (**b,c**) and positive (**d-f**) biases corresponding to resonances in the vibronic signal.

C_S in WSe_2

Experimental conditions for the dehydrogenation of CH_X for tungsten diselenide (WSe_2) are identical to those for WS_2, see Fig. S7. A significant difference between the two materials is that even though both $\mathrm{CH_S}$ and $\mathrm{CH_{Se}}$ are both negatively charged, upon hydrogen removal, $\mathrm{C_{Se}}$ becomes neutral, while $\mathrm{C_S}$ remains negatively charged. This is seen in STM imaging by the absence of a dark depression surrounding the defect due to the lack of band bending, see Fig. S1b (in addition to the lack of splitting of the in gap resonance discussed in the main text).

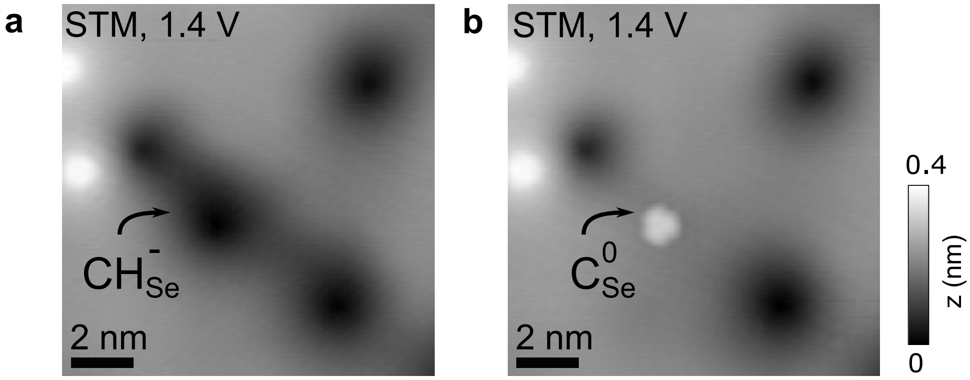

Figure S7. STM constant current topographic image of an **a** $\mathrm{CH_{Se}}$ and a **b** $\mathrm{C_{Se}}$ defect respectively. Scanning parameters: $V_B = 1.5$ V, $I_t = 100$ pA, 15 x 15 nm.

SUPPLEMENTARY CALCULATIONS

Electronic structure of the defect states

Fig. S8 shows our calculated density of states of the defect states with the integrated local density of states (ILDOS) that corresponds to the computed STM images. In particular, we project the defect wavefunction onto carbon atomic orbitals; carbon comprises about 33% of the defect state character. These states possess additional contributions from tungsten and sulfur states, indicating the defect states are hybridized (Fig. S9). ILDOS for the defect states (inset) closely resemble the experimental STM images. From our calculations, we find $m_j = +1/2$ ($m_j = -1/2$) for both $j = 3/2$ and $j = 1/2$ contribute to the occupied (unoccupied) state.

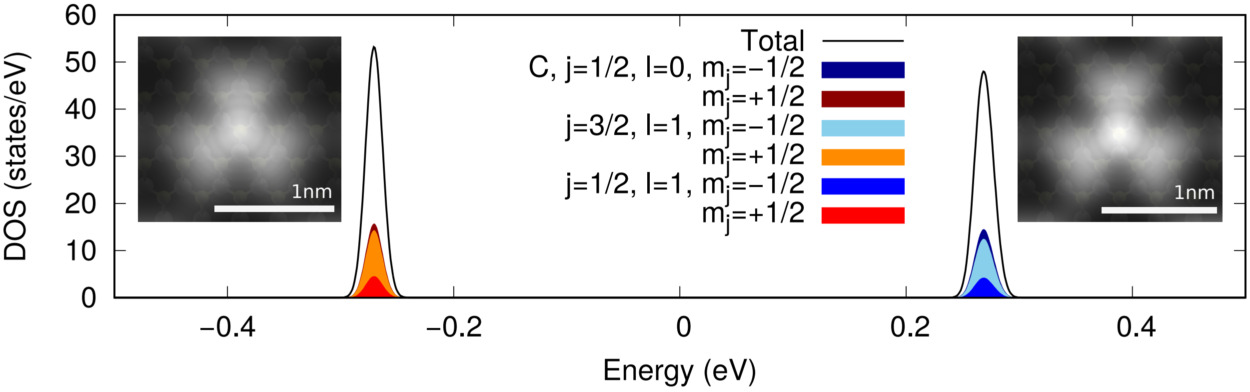

Figure S8. Projected density of states and integrated local density of states of the defect states calculated by PBE with SOC in 5×5 supercell. Carbon contributions are shown. The centroid of the defect states is taken to be the zero of energy. Insets are integrated local density of states of the occupied and unoccupied defect states, respectively.

Electronic structure of the CRI in monolayer and bilayer WS_2

Fig. S9 shows the projected density of state of the CRI in monolayer and bilayer WS_2, respectively. For our bilayer calculations, we use the LDA functional. The computed interlayer spacing, measured by difference in z-coordinate of W atom in each layer, is found to be 6.14 Å and the distance between top S in bottom WS_2 and bottom S in top WS_2 is found to be 3.04 Å. Defect level splitting is calculated to decrease in the bilayer.

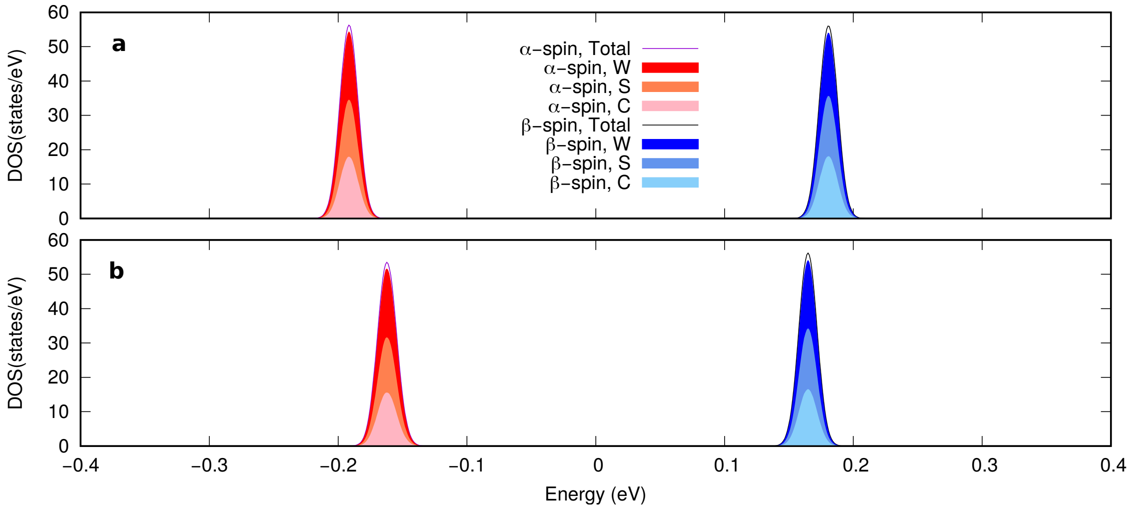

Figure S9. **a**,**b**, Projected density of states of the CRI in (**a**) monolayer and (**b**) bilayer WS_2 with 6×6 supercell without SOC using LDA.

Origin of the distinct vibronic coupling of the spin-split defect states

The STM images of the spin-split defect states, at first glance, seem to be nearly identical, but there are meaningful differences between them that result in distinct electron-phonon coupling behavior for each defect state. Fig. S10 shows the difference of the density of each defect state ($\Delta\rho = \rho_{\text{occupied}} - \rho_{\text{unoccupied}}$), where $\rho_{\text{occupied}} = |\psi_{\text{occupied}}|^2$. The green isosurface stems from an excess electron density of the unoccupied state that is concentrated on the three neighboring W, C and bottom S atoms. The unoccupied defect state shows strong coupling with the 22 meV mode that is characterized by a breathing-like movement of these atoms. The red isosurface resulting from an excess electron concentration of the occupied defect state is mainly concentrated on the C atom. This state shows stronger coupling with the 75 meV mode that is characterized by an out-of-plane oscillation of the C atom. Hence, the electron-phonon coupling strength is significant because the degree of the localization of the electronic wavefunction is sizable at the lattice sites where the vibration occurs.

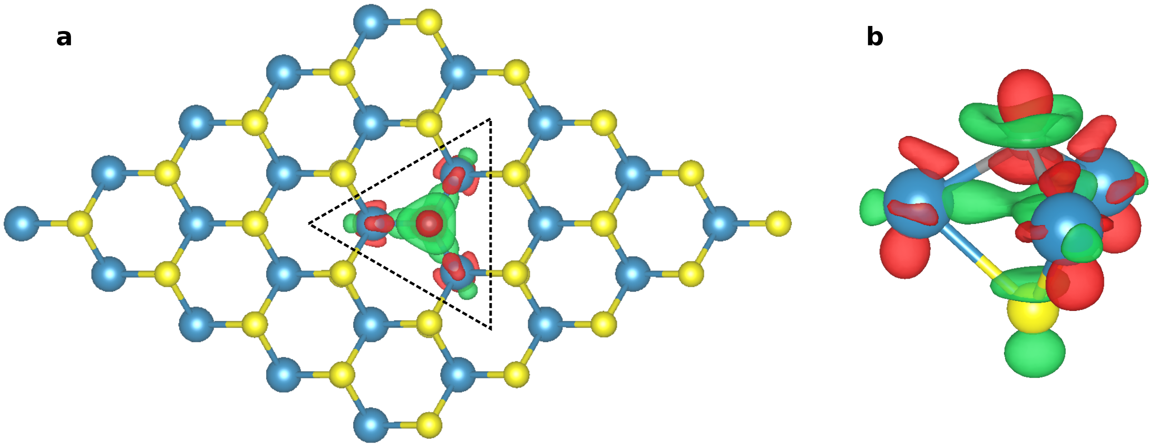

Figure S10. **a**, Top and **b**, perspective view of the difference of the defect states ($\Delta\rho$). The dashed triangle in (**a**) is highlighted in (**b**). Green (red) region has negative (positive) value and represents a distinct part that the unoccupied (occupied) defect state contributes. Isosurface is set to $\pm 0.8 \cdot 10^{-3} e/\text{Å}^3$

Defect wavefunction in bilayer WS_2

The defect wavefunction in bilayer WS_2 is not only localized in the layer that contains the carbon impurity, but also spreads in part into the bottom layer, particularly out to the W atom directly below the carbon impurity as shown in Fig. S11. Interlayer interactions lead to a slight delocalization of the defect state wavefunction.

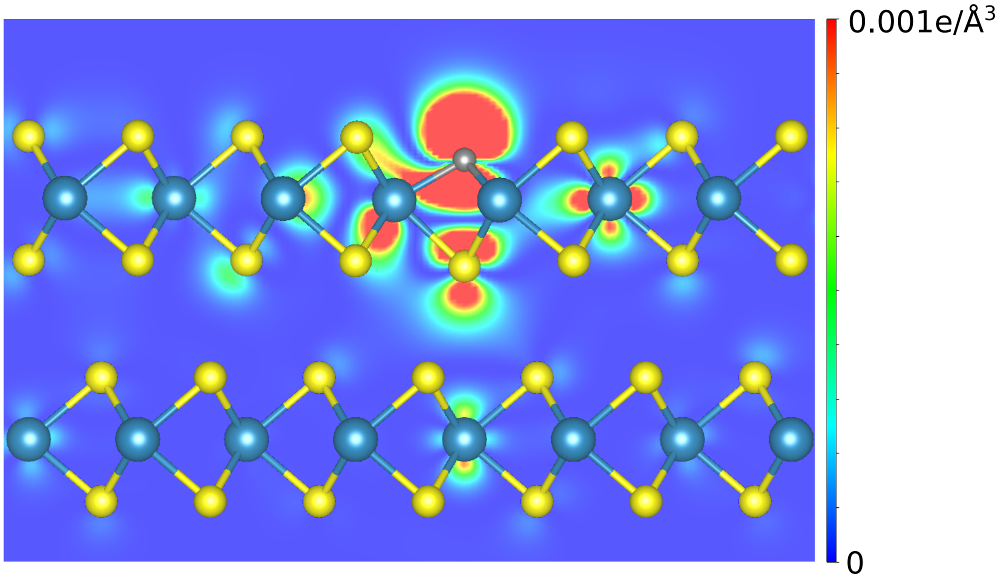

Figure S11. Defect wavefunction in bilayer WS_2 in a 2D plane that contains carbon-tungsten bonds.

Resonant low-energy phonon modes

We can categorize two types of phonon modes that yield a finite coupling strength: local and resonant modes. Local phonon modes exhibit a flat dispersion and their energy and displacement patterns converge rapidly with increasing supercell size. Resonant, long wavelength phonons are more difficult to describe with our calculations as the choice of supercell and associated periodic boundary conditions impose a specific sampling of the reciprocal space. As we generate a supercell that is commensurate with the primitive WS_2 cell, some $\mathbf{q}$-points of the primitive WS_2 cell are folded onto the Γ-point of the supercell. Thus, the Γ-point of each supercell contains *inequivalent* $\mathbf{q}$-points that can be described as shown in Fig. S12, unless the size of the two supercells can be connected by integer multiplication. This means that by enlarging the size of the supercell we are not necessarily converging the resonant mode energy and electron-phonon coupling; we are merely computing the electron-phonon coupling at the different $\mathbf{q}$-points. In order to describe the interaction between an isolated point defect energy level and a phonon bath, considering Γ-point phonons is sufficient, as we wish to minimize artificial interactions between periodic images of defects in neighboring supercells.

As mentioned in the main text, our calculations have identified that the resonant mode that manifests strong coupling with the occupied defect states is a so called flexural phonon mode with an out of plane amplitude. In our supercell calculation, the flexural phonon in the 6×6 supercell is unique, leading to larger S than for 5×5 and 7×7 supercells. There are flexural modes in the 5×5 and 7×7 supercells as well, but the coupling strength is much smaller than that in the 6×6 supercell.

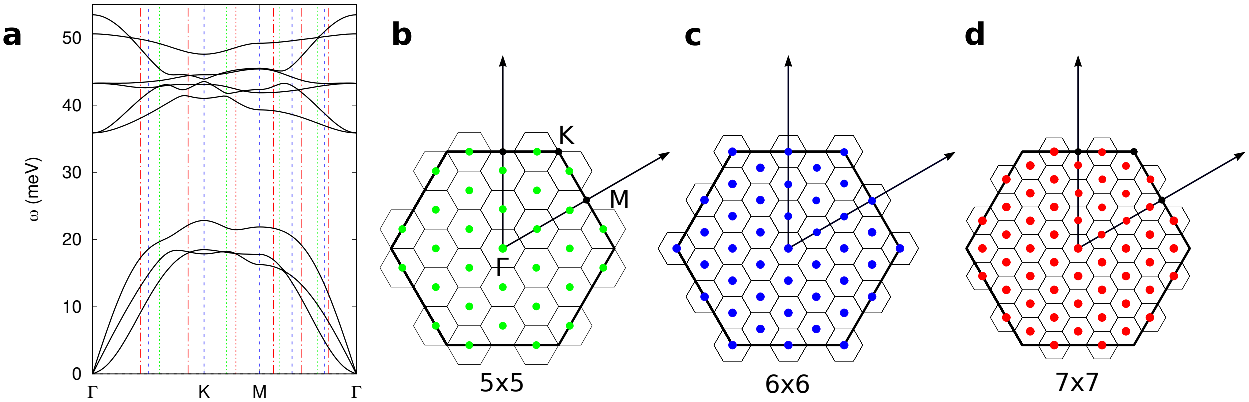

Figure S12. **a**, Phonon dispersion of the monolayer WS_2 with the vertical lines that correspond **q**-points that can be expressed in the supercells. **b-d**, Brillouin zone of (**b**) 5×5, (**c**) 6×6, and (**d**) 7×7 supercells in that of the 1×1 unit.

Convergence test

We performed convergence tests for the calculated energy gain by spin-polarization and Huang-Rhys factor as a function of the supercell size as follows. We first calculated the energy difference between nonmagnetic and spin-polarized ground state as a function of supercell size, shown in Fig. S13, that is

$$\Delta E_{\mathrm{sp-nm}} = E_{\mathrm{sp}} - E_{\mathrm{nm}}. \tag{S1}$$

We calculated $\Delta E_{\mathrm{sp-nm}}$ using PBE as a function of the supercell size as shown in Fig. S13a. $\Delta E_{\mathrm{sp-nm}}$ converges within 6 meV at the 6×6 supercell, which means the 6×6 supercell is sufficient to minimize the interactions between defects. The distance between CRIs in the 6×6

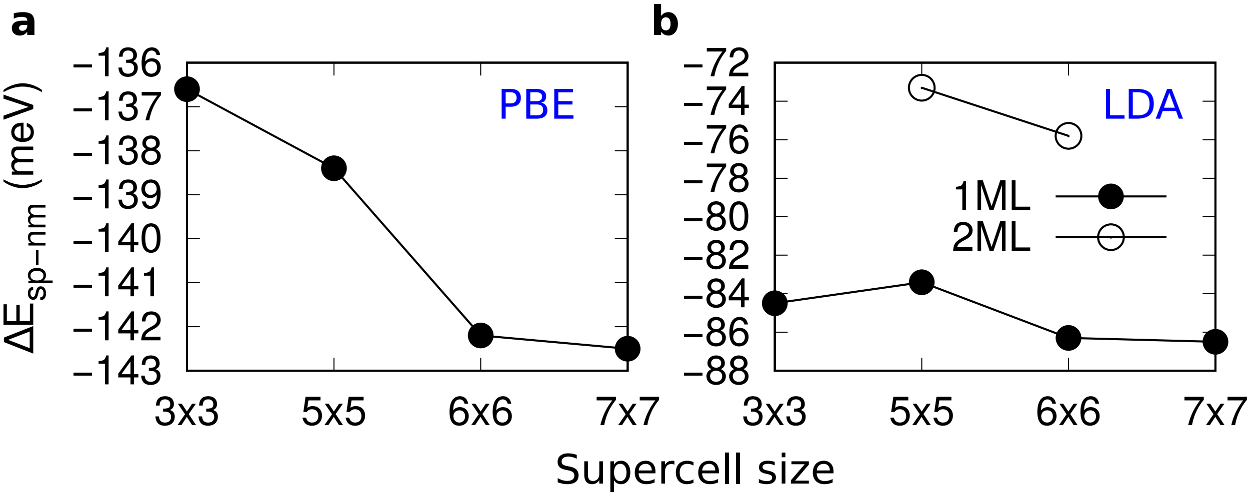

Figure S13. **a**,**b**, Calculated energy difference between the nonmagnetic and spin-polarized ground states with respect to supercell size using (**a**) PBE and (**b**) LDA functional, respectively. Filled (open) circles represent monolayer (bilayer) results.

is $\sim$ 18.9 Å, whereas in the 5×5, it is $\sim$ 15.8 Å. When we calculate $\Delta E_{\text{sp}-\text{nm}}$ using LDA, energy gain by spin-polarization is decreased by $\sim$ 56 meV (see Fig. S13b). LDA results also tend to converge at the 6×6 supercell. In the bilayer, $\Delta E_{\text{sp}-\text{nm}}$ is $\sim$ 10 meV smaller than in the monolayer.

We also calculated Huang-Rhys factor as a function of the supercell size for the local phonon modes as shown in Fig. S14. The calculated Huang-Rhys factor of the two local phonon modes converge at the 5×5 supercell.

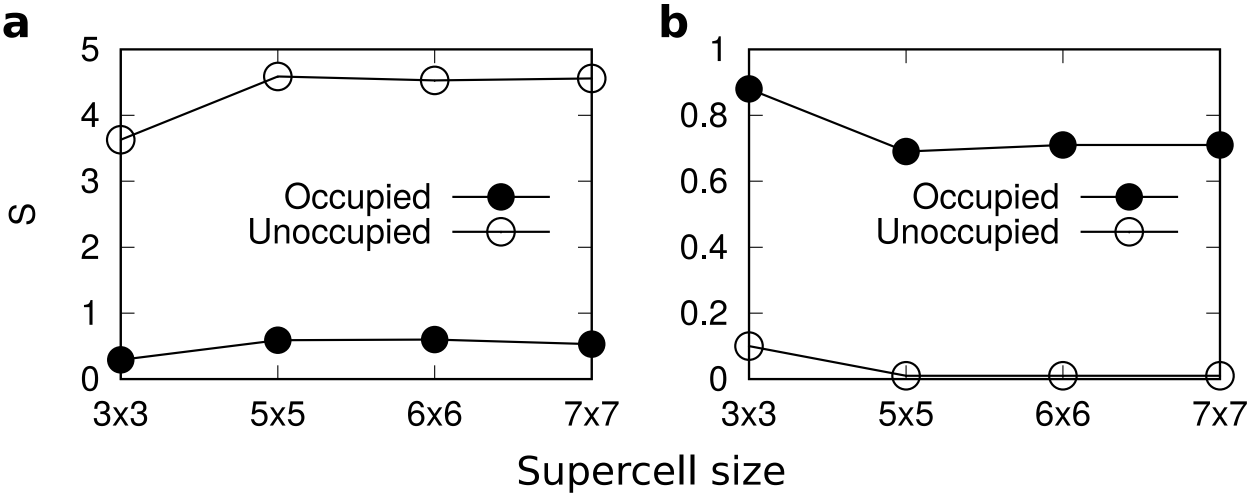

Figure S14. **a,b**, Calculated Huang-Rhys factors for (**a**) 22 meV and (**b**) 75 meV local phonon mode as a function of supercell

Functional dependence of Huang-Rhys factor

We calculated the Huang-Rhys factor using a PBE and a LDA functional, respectively, as shown in Fig. S15. We find that PBE tends to result in larger S values than those using LDA, except for the coupling between the occupied and the 22 meV local phonon mode. The calculated Huang-Rhys factors in the bilayer are weaker than those in the monolayer.

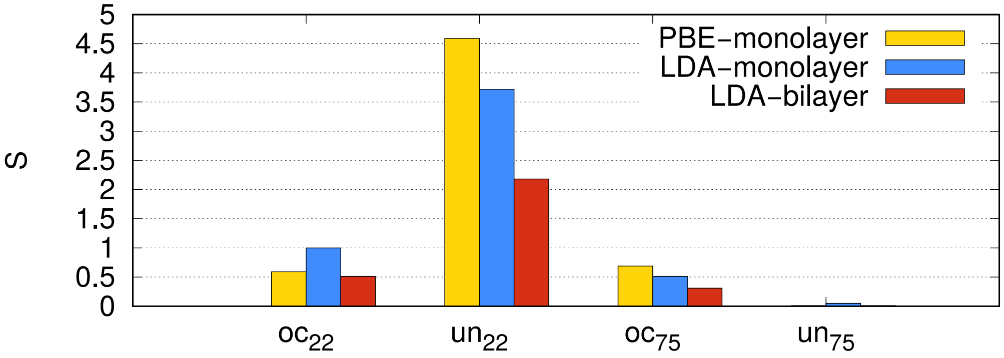

Figure S15. Calculated Huang-Rhys factor using PBE and LDA in a 5×5 supercell. oc$_{22}$ (un$_{75}$) stands for coupling between the occupied (unoccupied) defect state and 22 (75) meV local phonon mode. Bilayer results calculated by LDA are shown.

Valley splitting

We calculated λ $(= \epsilon_V^K - \epsilon_V^{K'})$ as a function of defect density, ρ, by changing supercell size, as shown in Fig. S16. For the sample defect densities, the valley splitting λ increases logarithmically as a function of magnetic defect density.

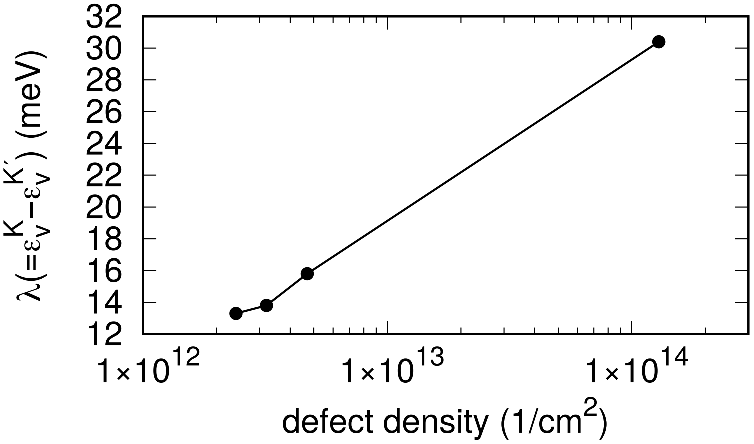

Figure S16. Calculated λ as a function of doping concentration. The highest (lowest) defect density corresponds to a 3×3 and (7×7) supercell, respectively.

---

* These authors contributed equally to this work.

† jbneaton@lbl.gov

‡ afweber-bargioni@lbl.gov

§ bruno.schuler@empa.ch

[1] Liu, H. *et al.* Molecular-beam epitaxy of monolayer and bilayer WSe_2: a scanning tunneling microscopy/spectroscopy study and deduction of exciton binding energy. *2D Materials* **2**, 034004 (2015).

[2] Aghajanian, M. *et al.* Resonant and bound states of charged defects in two-dimensional semiconductors. *Phys. Rev. B* **101**, 081201(R) (2020).